nature communications

Article

https://doi.org/10.1038/s41467-024-54810-0

Specific surface-modified iron oxide nanoparticles trigger complement-dependent innate and adaptive antileukaemia immunity

Received: 14 November 2023

Accepted: 22 November 2024

Published online: 29 November 2024

Check for updates

Yuanyuan Li[1,7], Wen Wu[1,7], Qihui Liu[1,7], Qiong Wu[1], Ping Ren[2,3], Xi Xi[1], Haiyan Liu[1,4], Jiarui Zhao[1], Wei Zhang[5], Zizhun Wang[5], Yuanyuan lv[1], Bin Tian[1], Shuang Sun[1], Jiaqi Cui[1], Yangyang Zhao[1], Jingyuan Wu[1], Mingyuan Gao[6] & Fangfang Chen[1,2]

Considerable advances have been achieved in the application of nanomaterials for immunotherapies, yet the precise immune effects induced by protein corona remain elusive. Here, we explore the formation mechanism and immune regulation process of protein corona in acute myeloid leukaemia (AML) mouse models using commercialized iron oxide nanoparticles (IONPs), with different surface modifications, including an FDA-approved variant. Using macrophages depleted or Complement Component 3 (C3) knockout mice, we demonstrate that carboxymethyl dextran-coated IONP (IONP-COOH) reduces leukaemia burden. Mechanistically, IONP-COOH indirectly binds to C3b after activating the complement alternative pathway, subsequently enhancing phagocytosis of macrophages and activating adaptive immunity mediated by complement corona. While aminated dextran-coated IONPs directly absorb C3b and activate the lectin pathway, leading to immune cell exhaustion. Our findings suggest that IONP-COOH may serve as an immune activator for AML treatment, offering a promising approach to developing therapeutic nanomaterials by leveraging surface chemistry to enhance immunotherapy.

Acute myeloid leukaemia (AML) is a heterogeneous disease with a poor prognosis, the overall 5-year relative survival rate is 29.5%[1–4]. While advancements have occurred in pathobiology and the identification of new therapeutic targets, the standard therapies for AML remained unchanged substantially in the past decades. Furthermore, with the involvement of chemoresistance-associated side effects, including cardiotoxicity, myelosuppression, and susceptibility to infections, conventional therapeutics consistently result in treatment failure or relapse, ultimately culminating in fatality due to the disease[5]. Therefore, there is a pressing and urgent need for the development of novel therapeutic strategies to address the challenge.

[1]Key Laboratory of Pathobiology, Ministry of Education, Nanomedicine and Translational Research Center, China-Japan Union Hospital of Jilin University, Changchun, China. [2]The Skaggs School of Pharmacy and Pharmaceutical Sciences, Department of Pharmaceutical Sciences, University of Colorado Anschutz Medical Campus, Aurora, CO, USA. [3]Department of Thoracic Surgery, The First Hospital of Jilin University, Changchun, China. [4]Department of Anatomy, College of Basic Medical Sciences, Jilin University, Changchun, China. [5]Electron Microscopy Center, Jilin University, Changchun, China. [6]State Key Laboratory of Radiation Medicine and Protection, Collaborative Innovation Center of Radiation Medicine of Jiangsu Higher Education Institutions, School for Radiological and Interdisciplinary Sciences, Soochow University, Suzhou, China. [7]These authors contributed equally: Yuanyuan Li, Wen Wu, Qihui Liu.
e-mail: cff@jlu.edu.cn

Nanoparticles (NPs)-based immunotherapy can be used to promote or restore effective antitumour immune responses[6–10]. Recent studies have demonstrated the macrophage activation potency of ferumoxytol, an FDA-approved IONP formulation. Ferumoxytol has been shown to modulate macrophage phenotype and function, thereby enhancing antitumour immunotherapy[11,12]. These findings underscore the potential of IONP in modulating immune responses. Nonetheless, how macrophages were activated and their effects on other kinds of immune cells have yet to be elucidated. NPs-biological system interactions are mainly dependent on the physical and chemical properties of NPs, including the size, shape, surface charge, precise compositions and chemical stability[13–17]. In general, NPs can be endowed with a new biological identity due to the formation of a protein layer surrounding the NPs in the bioenvironment, termed protein corona (PC)[18], which can engage with receptors on immune cells and trigger signal cascades to activate the immune system[19].

Complement C3 and IgG are key components of the PC, facilitating the opsonization of NPs and leading to the recognition and engulfment of NPs by immune cells[20–22]. Additionally, the activation of complement components such as C3a and C5a, which bind to their respective receptors (C3aR and C5aR1), can trigger allergic reactions. The C5a-C5aR1 axis, in particular, plays a crucial role in mediating inflammatory responses. C5aR1 is primarily expressed on neutrophils, mast cells and eosinophils. Similarly, C3aR is expressed on various cell types including mast cells, basophils, eosinophils and endothelial cells. The binding of C3a and C5a to their receptors can result in the release of histamine from mast cells and the secretion of chemokines, contributing to inflammatory and immune responses[23,24]; C3b interact with CR3 on macrophages and granulocytes promotes the phagocytosis of immune complexes[25]; IgG only can induce phagocytosis by recognising FcγRs express on neutrophils, dendritic cells and macrophages[26,27]. Therefore, the immune PC on the NPs will induce a different immune response, thus providing a new strategy for immunotherapy with higher specificity and biosafety.

Here, we used six well-characterised dextran-coated IONPs to investigate the interaction with the immune system in the context of an AML model. We demonstrated that IONPs-COOH displays antileukemia effects through enhancing macrophage-mediated phagocytosis of tumour cells in a complement-dependent manner. Subsequently presenting tumour antigens to initiate adaptive antitumor immunity. IONPs-NH_2 and IONPs-OH, modified with amino and hydroxyl functional groups respectively, do not exhibit anti-leukaemia effects. This discrepancy is attributed to the distinct PCs formed on these NPs, which elicit varying immune responses that differ from those provoked by IONPs-COOH. These findings emphasise the critical role of the surface functional group of NPs in regulating their interactions with immune cells, thereby exerting a profound influence on their biological outcomes, which holds great potential for advancing the development of nanoparticle-based immunotherapies.

Results

IONP-COOH^{-21} inhibited leukaemia progression by indirectly killing

It was previously demonstrated that iron oxide NPs could increase oxidative stress and cell death of AML cells[28]. To this end, we further analyzed the role of IONP-COOH^{-21} in the regulation of AML cell death. We incubated murine-derived leukaemia cells (GFP$^+$) with IONP-COOH^{-21} for 24 h and measured apoptosis via Annexin-V/7AAD staining. The results revealed that there was no increase in apoptosis (Fig. 1A), note that even high concentrations of IONP-COOH^{-21} did not affect tumour cell proliferation (Fig. 1B). Thus, IONP-COOH^{-21} demonstrated no direct cytotoxic effects on leukaemia cells.

We next evaluated the therapeutic effect of IONP-COOH^{-21} in a human AML xenograft model, which was established using NSG mice transplanted with MOLM-13 cells that express human CD45 specifically. Mice with a tumour burden in the bone marrow exceeding 10% were administered intravenously (IV) with saline, or IONP-COOH^{-21} at a single dose of 6 mg kg^{-1}, respectively. The mice were euthanised and leukaemic blasts were evaluated in the bone marrow (BM) and spleen (SPL) at 24 h post-IONPs injection. Remarkably, compared with the saline group, leukaemic blasts were reduced in both Bone marrow (BM) and spleen after IONP-COOH^{-21} treated (30.9% vs 13.3% in BM and 36.1% vs 22.2% in SPL), considering both the percentage and the absolute number of leukaemic blasts (Fig. 1C–E). Additionally, The MFI of CD80$^+$ splenic macrophages were upregulated in response to IONP-COOH^{-21} stimuli, which contributed to the antileukaemia effect (Supplementary Fig. 1).

Furthermore, mice were then monitored to evaluate survival time. As shown in the study flowchart (Fig. 1F), the mice received either saline or IONP-COOH^{-21} starting from the 3rd day post MOLM-13 cell implantation, twice a week, for a total of three administrations. The survival was monitored and recorded and the data were plotted against days. IONP-COOH^{-21} treatment significantly improved overall survival, extending the median survival from 16 days to 19 days (Fig. 1G). These findings not only demonstrated an antileukaemia effect with IONP-COOH^{-21} administration but also showed a prolonged overall survival. Taken together, IONP-COOH^{-21} inhibited leukaemia progression by indirectly killing, which prompted us to focus on the direct effects of IONP-COOH^{-21} on immune cells in modulating antitumour immunity.

IONP-COOH^{-21} triggered both innate and adaptive immunity against acute myeloid leukaemia in a complement-dependent pattern

To gain further insights into the immune modulation by IONP-COOH^{-21}, we utilised another leukaemia mouse model with sound immune systems to investigate its regulation on the immune system. The system employed co-expression of the BCR-ABL and Nup98-HOXA9 translocations, which were monitored using green fluorescent protein (GFP). These translocations were commonly detected in human chronic myeloid leukaemia blast crisis and the model has previously been described for research on leukaemia genetics and stem cell biology[29,30], the target organs, aggressive nature and even chemoresistance of this model are similar to those of human AML[28]. Specifically, C57BL/6N mice were transplanted with these leukaemic cells and treated with either saline or IONP-COOH^{-21} on day 3 and 8. Leukaemic cells were detected in the spleen and bone marrow on day 10. According to Supplementary Fig. 2, the spleens of successfully modelled mice are significantly larger than those of normal mice, clearly indicating successful modelling. Consistent with the results shown in Fig. 1, IONP-COOH^{-21} treatment significantly suppressed the tumour burden in the bone marrow (7.76% vs 17.04%) and spleen (12.23% vs 22.58%) (Fig. 2A, B). This effect was also observed in female mice (Supplementary Fig. 3). These encouraging results demonstrated that the suitability of the C57BL/6N model as a valuable platform for studying the mechanisms underlying the antileukaemic immune response.

Given the absence of lymphocytes in NSG mice and our previous findings showing that IONP-COOH^{-21} exhibited specific interactions with macrophages (Supplementary Fig. 1), we directed our attention to exploring the potential roles of macrophages in C57BL/6N model. Macrophages are important components of the innate immune system in tissue remodelling, inflammation and immunity, including endocytosis of foreign and necrotic debris, cytotoxicity and secretion of multiple cytokines[31]. Consequently, we sought to investigate the impact of macrophage by depleting them through intraperitoneal injection of clodronate liposomes (Supplementary Fig. 4), Upon successful depletion of macrophage, IONP-COOH^{-21} no longer exhibited a reduction in the tumour burden in bone marrow, spleen (Fig. 2C) and peripheral blood (Supplementary Fig. 5). These data unequivocally

https://doi.org/10.1038/s41467-024-54810-0

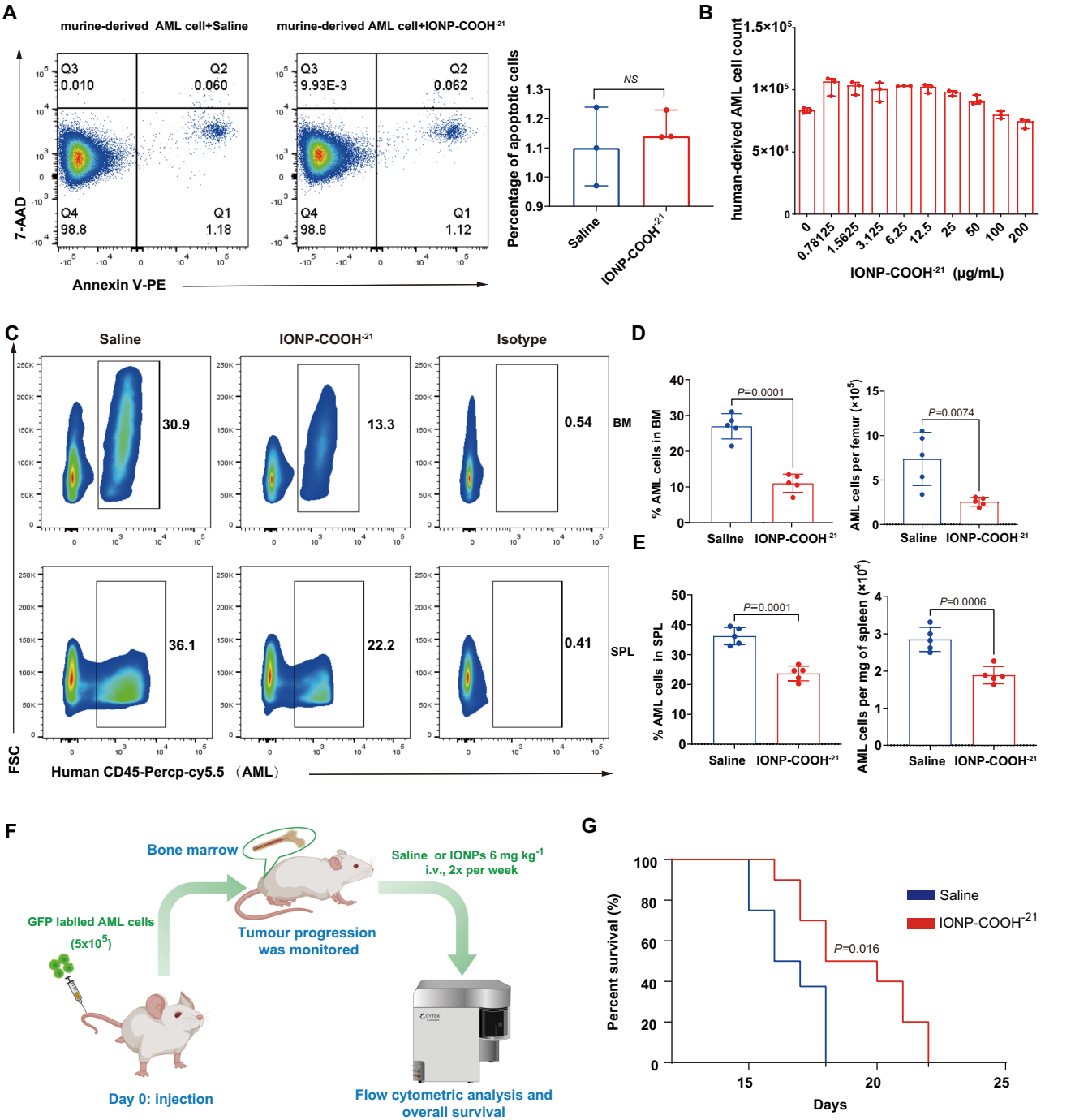

Fig. 1 | IONP-COOH^{-21} inhibited leukaemia progression by indirectly killing. **A** The apoptosis analysis of BCR-nup cells incubated with IONP-COOH^{-21} at 200 μg mL^{-1} for 24 h ($n = 3$ technical replicates; the experiment was independently repeated on three different days), apoptosis ratio (%) = Q1 + Q2. **B** Number of MOLM-13 cells after co-incubation with IONP-COOH^{-21} for 24 h at different iron concentrations ($n = 3$ technical replicates; the experiment was independently repeated on three different days), data of (**A**, **B**) are represented as mean ± SD. **C**–**E**, AML mice were injected (IV) with saline or IONP-COOH^{-21} 6 mg kg^{-1} on day 11, and tumour burden was analyzed on day 12 (n = 5 mice). The leukaemic cells were identified by human CD45^{+} expression. Experimental scheme (**F**) and Kaplan-Meier survival curves (**G**) for the effect of IONP-COOH^{-21} on overall survival ($n = 10$ mice/group), created in BioRender. https://BioRender.com/o33l748. Unpaired two-tailed *t*-tests were used in (**A**–**E**). Survival curves were compared using a log-rank Mantel-Cox test. Source data are provided as a Source Data file.

demonstrated the essential role of the macrophage in the antileukaemia efficacy of IONP-COOH^{-21}.

This observation also prompted us to explore how crosstalk functions between IONP-COOH^{-21} and macrophages. In physiological conditions, macrophages express high levels of complement receptors and produce complement components[32]. And previous studies also showed that tissue-resident macrophages could capture and digest circulating leukaemia cells via phagocytosis[33]. We thus assumed that IONP-COOH^{-21} triggered macrophage phagocytosis through complement opsonization. The mouse-derived leukaemia cell phagocytosis experiment was performed using macrophages stimulated by IONP-COOH^{-21} preincubated with plasma obtained from C57BL/6N or C3 KO mice (B6.129S4-C3tm1Crr/J). The results showed that preincubation with normal plasma increased the percentage of phagocytosis, while

https://doi.org/10.1038/s41467-024-54810-0

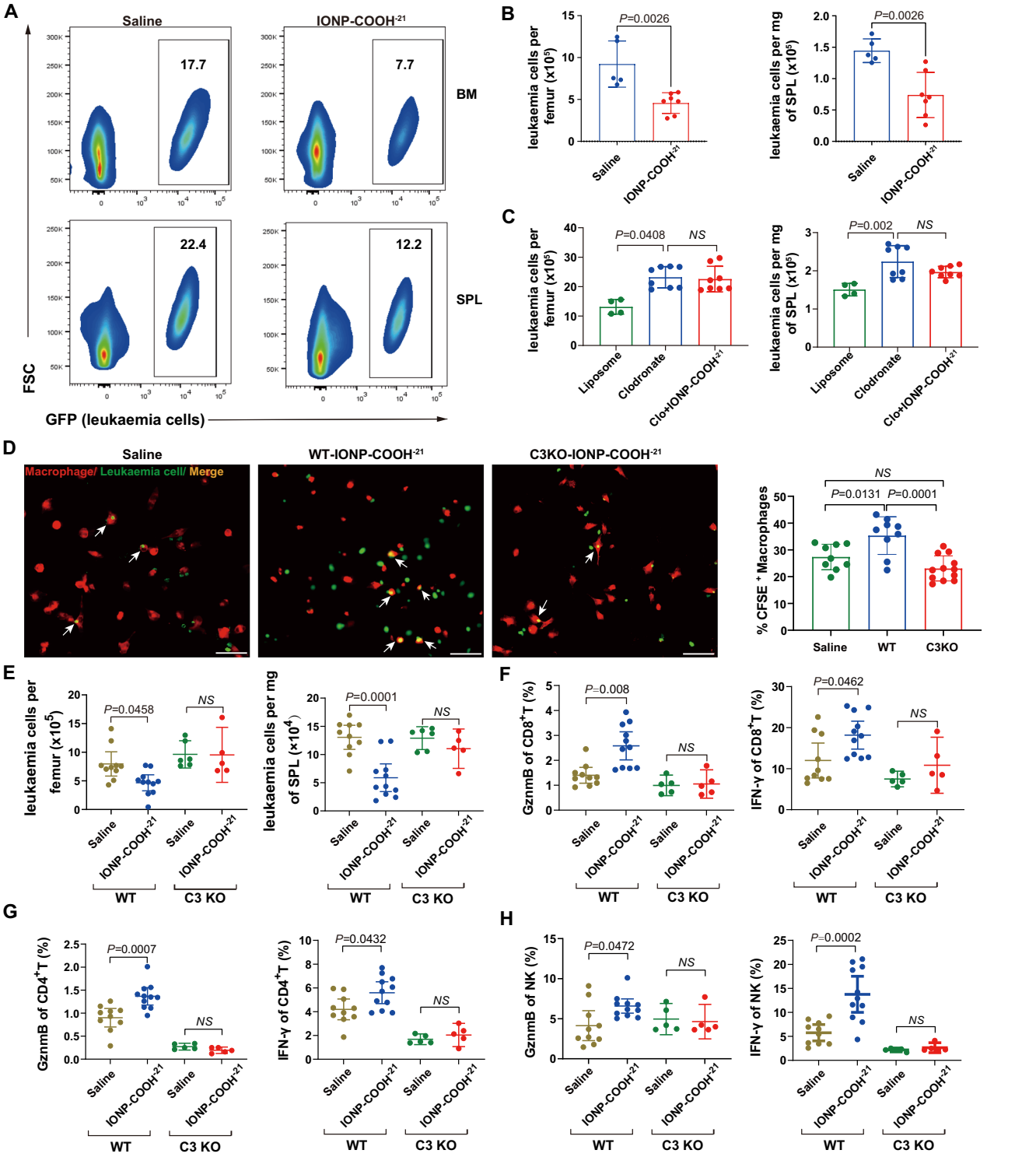

Fig. 2 | IONP-COOH^{-21} suppressed myeloid leukaemia progression in a complement-dependent manner. C57BL/6N AML mice were treated with saline ($n = 5$ mice) or IONP-COOH^{-21} at 6 mg kg^{-1} ($n = 7$ mice) on days 3 and 8. The percentage (**A**) and absolute cell counts (**B**) of leukaemia cells were analyzed on day 10. **C** Number of tumour cells after depleted macrophages. $n = 4$ mice, liposome control; $n = 8$ mice, clodronate group and IONP-COOH^{-21}-treated group. **D** Red, macrophages, F4/80-PE; Green, leukaemia cells, CFSE; White, macrophages engulfed leukaemia cells. Scale bar, 50 μm. $n = 9$ technical replicates, saline and IONP-COOH^{-21}-treated WT groups; $n = 12$ technical replicates, C3KO group. Primary cells were isolated from five mice, and the experiment was independently repeated on three different days. **E** Counts of leukaemic cell. Percentage of Granzyme B and IFN-γ in CD8$^+$, CD4$^+$ T (**F**, **G**) and NK cells (**H**). **E**–**H**. $n = 10$ mice, saline- WT; $n = 11$ mice, IONP-COOH^{-21}- WT; $n = 5$ mice, C3 knockout. All data are presented as mean ± SD. A two-tailed t-test was used in (**B**). One-way ANOVA with multiple comparison adjustments was applied in others. Source data are provided as a Source Data file.

C3-depleted plasma did not influence the phagocytosis (Fig. 2D). Consistently, similar trends were observed in the phagocytosis of human-derived leukaemia cells (Supplementary Fig. 6). In addition, the results of Supplementary Fig. 7 showed IONP-COOH^{-21} induced proinflammatory M1 macrophage polarisation in vitro, which contributed to macrophage phagocytosis. Collectively, these observations provided strong evidence that IONP-COOH^{-21} inhibited AML by triggering macrophage phagocytosis in a C3-dependent manner.

We next employed C3 KO mice to evaluate the role of complement in the crosstalk between IONP-COOH^{-21} and the immune system. As expected, the depletion of C3 resulted in a complete loss of the antileukaemia effect of IONP-COOH^{-21} in both bone marrow and spleen (Fig. 2E). Furthermore, IONP-COOH^{-21} significantly increased the percentage of Granzyme B and IFN-γ in NK, CD4^{+}T and CD8^{+}T cells in C57BL/6N mice. Notably, these increases were abolished in C3 KO mice as shown in Fig. 2F-H. Granzyme B and IFN-γ are critical effectors and messenger molecules in adaptive antitumour immunity[34,35]. Based on these results, we concluded that IONP-COOH^{-21} can elicit both innate and adaptive immunity in a complement-dependent manner to antileukaemia.

Physicochemical characterisation and antileukaemia effects of iron oxide nanoparticles with various surface residues

To understand if such an effect applies to other iron oxide NPs, we screened a series of dextran-coated IONPs with various surface residues, within the context of a murine model of AML. The detailed information on the physicochemical properties of the IONPs adopted in this study is given in Table 1 and Supplementary Fig. 8. The surface structures of the IONPs were investigated by X-ray photoelectron spectroscopy (XPS). The appearance of the N signal and the significant increase of the carboxyl signal confirmed the presence of NH_2 and -COOH residues on the NPs denoted as IONPs-OH (Fig. 3A and Supplementary Fig. 9A). All IONPs showed comparable sizes, interestingly, the zeta-sizer measurement revealed a 10- to 20-fold increase in the hydrodynamic diameter of IONP-NH_2 after incubating with human plasma (Fig. 3B and Supplementary Fig. 9B), and IONP-COOH exhibited a 2-fold increase, the quality of hard PC consistently correlated with their thickness (Supplementary Fig. 10). Moreover, the FTIR spectra of the carboxyl-functionalized materials exhibit a distinct stretching vibration peak at 1737 cm^{-1}, corresponding to the C=O bond, which is typical for carbonyl groups. A broad absorption band between 3200–3400 cm^{-1} is observed across all spectra, indicating the presence of O–H stretching vibrations, a consistent feature attributed to the dextran coating with numerous hydroxyl groups. Although N-H stretching vibrations generally appear in the same region as O–H vibrations (3200–3410 cm^{-1}), distinguishing between these groups using FTIR alone is challenging. Therefore, a fluorescent amine-reactive dye was utilised, revealing that the two amine-functionalized materials exhibit yellow-green fluorescence under UV light. Sample 4 shows less fluorescence than sample 3, indicating a lower degree of amine functionalization. Overall, the similarity in the FTIR spectra across all materials is primarily due to the characteristic absorption peaks of dextran, which dominate the spectral features (Supplementary Fig. 11). In selecting these materials, we ensured the consistency of the iron core across different variants. Multiple analyses, including transmission electron microscopy (Supplementary Fig. 12), inductively coupled plasma and NanoSight analysis (Supplementary Fig. 13), confirmed that the internal iron cores of the NPs are ~6–8 nm in size, with an iron core content of about 0.05–0.06 pg per particle. The selected IONPs contain an internal structure of magnetite (Fe_3O_4). XPS analysis of the iron core revealed that the materials modified with the three different functional groups exhibited highly similar Fe $2p_{1/2}$ and Fe $2p_{3/2}$ peaks, with binding energies corresponding to the coexistence of Fe^{2+} and Fe^{3+} oxidation states. The consistency in these peak positions and relative intensities across all samples indicates that the surface modifications did not alter or damage the integrity of the iron core (Supplementary Fig. 14). These findings confirm that the functionalization processes preserved the core's physical and chemical properties, ensuring the comparability of the IONPs for further applications.

To explore the immunotherapeutic potential of these IONPs, with the same treatments as Fig. 1C, mice were administered intravenously (IV) with saline, IONP-OH^{-4} and IONP-NH_2^{+44}, at a single dose of 6 mg kg^{-1}, respectively. The mice were euthanised and leukaemic blasts were evaluated in the bone marrow (BM) and spleen at 24 h post-IONPs injection. These IONPs did not display any therapeutic effects (Fig. 3C, D). Taken together, these findings confirmed that not all dextran-coated iron oxide NPs were equally effective in AML, the treatment effects may also be related to the surface residues of IONPs.

The activation pathway and variability of the complement system for various surface residues modified IONPs

Following the observations of the differences in size and zeta potential after incubation with plasma, we speculated that various surface residues modified IONPs could adsorb different plasma after entering the blood, which was crucial to the subsequent immunotherapeutic potential to IONPs in vivo. Thus, we next analyzed the composition of the PC formed on the different IONPs using liquid chromatography-mass spectrometry (LC-MS). The three-dimensional (3D) principal component analysis (PCA) plot showed a distinct clustering among the

Table 1 | Characterisation of IONPs used in the study (average of 3 measurements)

Particle ID		I	II	III	IV	V	VI
Product Name		Molday ION	Molday ION -	Molday ION Rhodamine B	Molday ION Dye Free	Feraheme®(FDA)	Molday ION Carboxyl Terminated
Abbreviation		IONP-OH^{-4}	IONP-OH^{-16}	IONP-NH_2^{+30}	IONP-NH_2^{+44}	IONP-COOH^{-21}	IONP-COOH^{-34}
Surface coating		10 kDa native dextran	10 kDa native dextran	10 kDa native dextran	10 kDa native dextran	10 kDa carboxymethyl-dextran	10 kDa carboxymethyl-dextran
Zeta potential (mV)		−4.40 ± 0.47	−15.70 ± 1.37	30.20 ± 1.16	44.00 ± 2.14	−20.80 ± 0.84	−34.30 ± 2.25
DI water (nm)	−	29.71 ± 2.28	29.04 ± 1.75	33.96 ± 3.37	34.46 ± 0.05	32.49 ± 1.54	34.42 ± 0.63
	+	42.55 ± 2.79	55.28 ± 0.18	617.10 ± 18.83	387.80 ± 41.01	57.05 ± 0.80	47.96 ± 0.58
PBS (nm)	−	32.44 ± 3.66	34.77 ± 0.51	41.29 ± 1.85	44.90 ± 0.47	33.49 ± 3.34	36.43 ± 5.44
	+	47.90 ± 4.61	36.19 ± 3.72	389.90 ± 97.09	214.10 ± 9.88	66.42 ± 3.74	64.39 ± 9.06
1640 Medium (nm)	−	32.68 ± 0.30	29.87 ± 0.06	44.36 ± 1.87	42.96 ± 0.15	28.91 ± 0.50	41.84 ± 1.98
	+	43.73 ± 10.03	32.79 ± 3.47	336.50 ± 35.09	172.60 ± 14.33	51.35 ± 2.07	53.22 ± 5.20

−. Before plasma incubation; +. After plasma incubation. Nanoparticles I, II, III, IV and VI were purchased from the Biophysics Assay Laboratory (USA). Nanoparticles V, IONP-COOH^{-21} (Feraheme®), an FDA-approved drug for the treatment of iron deficiency in patients with renal impairment, was provided by the University of Colorado Hospital Pharmacy.

https://doi.org/10.1038/s41467-024-54810-0

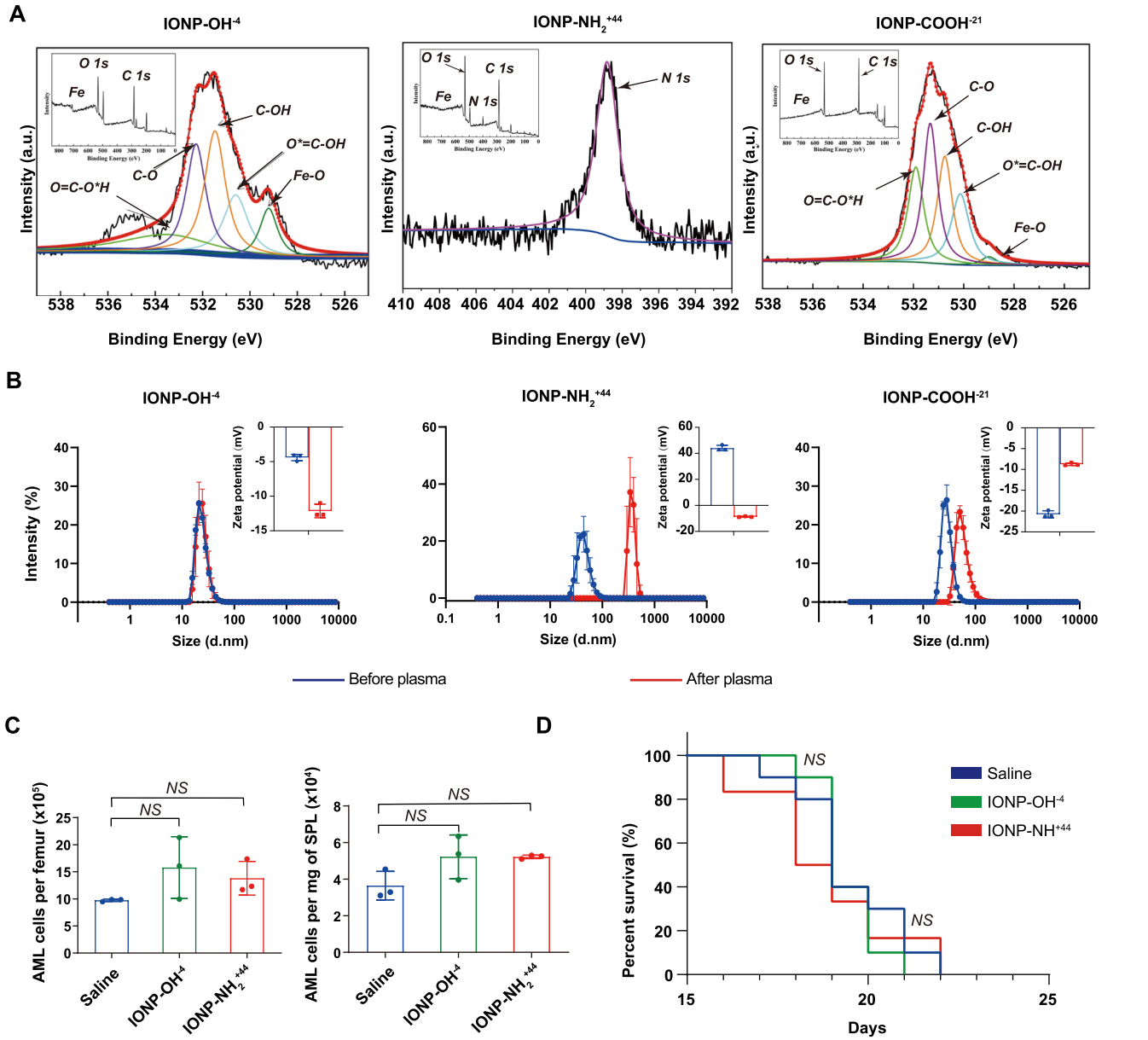

Fig. 3 | Physicochemical characterisation and antileukaemia effects of IONPs. **A** XPS analysis of high-resolution O1s spectrum of IONP-OH and IONP-COOH and high-resolution N1s spectrum of IONP-NH_2. The XPS survey spectra of the corresponding nanomaterials were presented in the inset. **B** The hydrodynamic size and zeta potential of IONPs were assessed both before (blue) and after (red) incubation with human plasma. The IONPs were incubated with human plasma and washed three times. Each experiment was repeated twice using samples obtained from three different donors, with three technical replicates performed for each measurement. **C** NSG mice were inoculated intravenously (IV) with 5×10^5 MOLM-13 cells to establish an AML mouse model. The mice were injected (IV) with saline or IONPs 6 mg kg^{-1} on day 11 and the tumour burden was analyzed by flow cytometry on day 12 ($n = 3$ mice/group). The absolute numbers of AML cells were calculated by multiplying the frequency of human $CD45^+$ cells by the total concentration of splenic cells or bone marrow cells from the femur. Bars represent the mean, and error bars represent SD. One-way ANOVA with multiple comparison adjustments was applied in (**C**). **D** NSG mice treated with saline or 6 mg kg^{-1} of IONPs by ($n = 10$ mice/group), survival curves were analyzed using the Kaplan-Meier method. Source data are provided as a Source Data file.

three types of NPs, highlighting their differences. Additionally, the plot revealed a noticeable similarity between the two NPs with the same modification (Fig. 4A). By LC-MS, we identified 697, 721 and 734 proteins on IONP-OH^{-4}, IONP-NH_2^{+44} and IONP-$COOH^{-21}$, respectively (Fig. 4B). Notably, immunoglobulin, coagulation factors, apolipoproteins and complement proteins were the most frequently identified proteins. Immunoglobulin and complement proteins play critical roles in immune response and phagocytosis[20]. The complement components constituted variable proportions of the PC on IONP-OH^{-4} (4.7%), IONP-NH_2^{+44} (4.3%) and IONP-$COOH^{-21}$ (8.6%). The above results demonstrated that surface residue can give rise to different compositions for the immune PC, which may subsequently regulate their interactions with the immune system (Fig. 4B, C).

Typically, NPs can activate the complement system through all three pathways[36] (Fig. 4D). To further analyze the biological pathways involved, a comprehensive bioinformatic pathway analysis was conducted on the top 20 most abundant proteins based on the Kyoto Encyclopaedia of Genes and Genomes (KEGG) pathway database. Interestingly, the results showed that the complement and coagulation cascade was notably different among the three types of IONPs (Fig. 4E). Therefore, we determined the complement components on three types of IONPs, and the number of properdin molecules per IONP-

https://doi.org/10.1038/s41467-024-54810-0

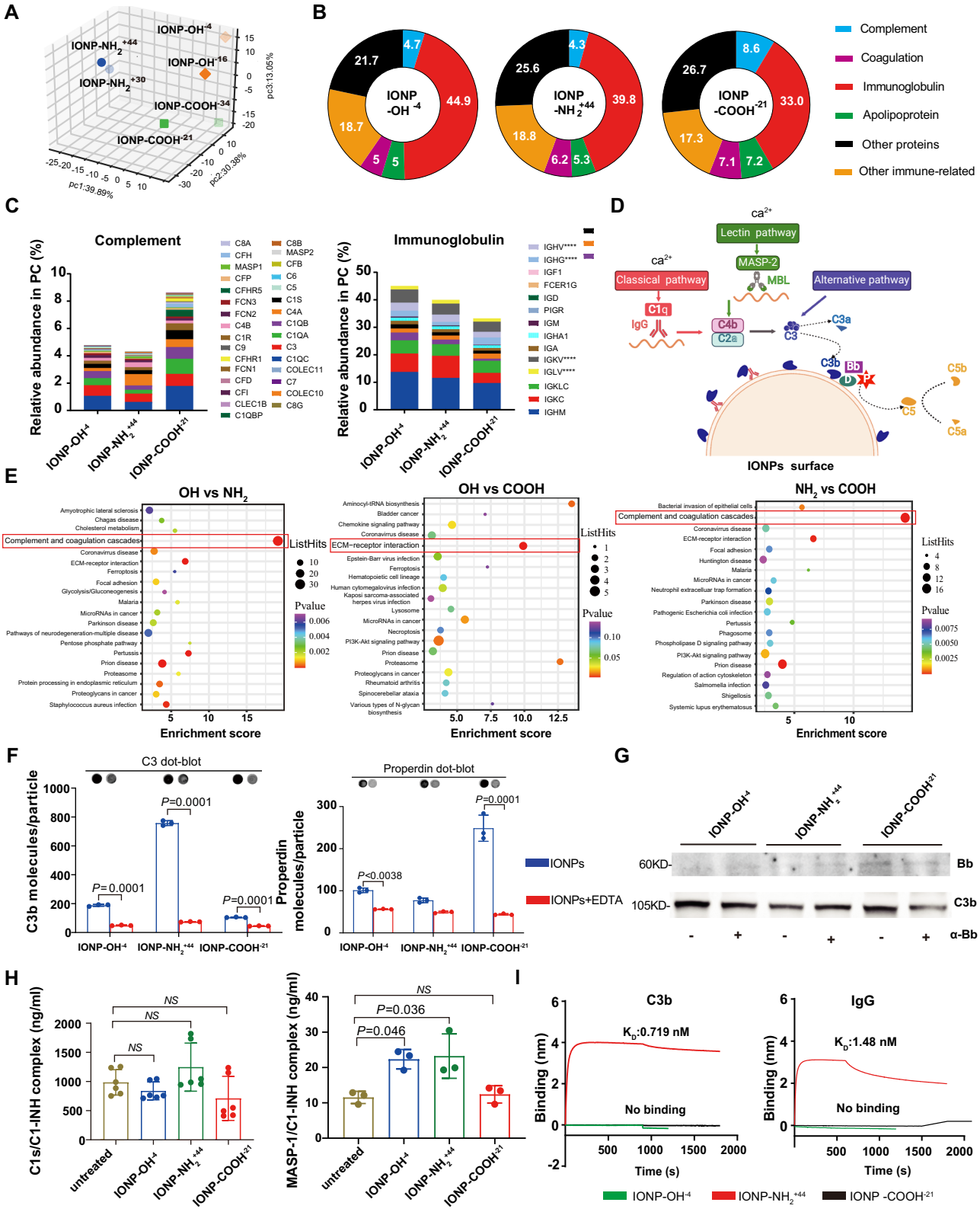

$COOH^{-21}$ was two-fold higher than others, but the deposition of C4b on IONP-$COOH^{-21}$ was significantly lower than the other two types of IONPs, an average 1.6- and 3.2-fold difference in mean fluorescence intensity was observed (Fig. 4F and Supplementary Fig. 15). In addition to utilising healthy human plasma, we conducted parallel experiments with plasma derived from AML patients and an AML C57 mouse model (Supplementary Figs. 16–18). The C3b protein levels adsorbed on the IONP surfaces were quantitatively analyzed. The results confirmed higher C3b adsorption on amino-modified IONPs, with overall increased levels when using AML patient plasma compared to healthy controls (Supplementary Fig. 17). This underscores the influence of disease-specific conditions on PC composition. The sex of the plasma donors (both male and female) was documented and considered in the analysis.

In order to prove specific pathways activation, the pathway specific soluble markers Bb, C1s/C1-INH and MASP-1/C1-INH were

Fig. 4 | IONPs with different functional groups activated the complement system through distinct complement pathways. A 3D PCA for protein. **B–C** Protein corona was identified by LC-MS. **D** Scheme of complement pathways (Created in BioRender. https://BioRender.com/b64n273). **E**, Bioinformatic pathway analysis for top 20 proteins based on KEGG pathway database. **F** Quantitative assay of C3b and properdin number per IONP. The dots represent individual data points corresponding to plasma samples collected from three different individuals ($n = 3$ healthy donor samples, biological replicates). The experiment was independently repeated three times. Data were evaluated by two-way ANOVA with multiple comparison adjustments. **G** Western blot of Bb/C3b after incubation with AML plasma. Samples were derived from the same experiment batch but different gels for Bb, and another for C3b were processed in parallel. The experiment was repeated three times independently with similar results. **H** ELISA detection of C1s/C1-INH and MASP/C1-INH complexes. The dots represent individual data points corresponding to plasma samples collected from different individuals ($n = 6$ healthy donor samples for C1s/C1-INH, $n = 3$ healthy donor samples for MASP/C1-INH, all representing biological replicates). The experiment was independently repeated twice. Data were evaluated by one-way ANOVA with multiple comparison adjustments. **I** Curves of the C3b/IgG and IONPs by biolayer interferometry. Source data are provided as a Source Data file.

employed. As shown in Fig. 4G, the level of Bb adhered to the surface of IONP-$COOH^{-21}$ was significantly higher than that of the other two IONPs. Additionally, when we pre-incubated plasma with Bb antibodies to block AP pathway activation, the amount of C3b adhered to the surface of IONP-$COOH^{-21}$ was significantly reduced, with an inhibition rate of up to 40%. These findings align with our previous properdin detection results, supporting the efficient activation of the AP pathway for carboxyl-modified IONPs. Furthermore, for CP and LP pathways, we measured the specific markers C1s/C1-INH and MASP-1/C1-INH (Fig. 4H). Our results demonstrated that hydroxy- and amino-modified IONP treatments led to a significant increase (2–3 fold) in plasma MASP-1/C1-INH levels compared to the untreated group. These findings suggest that hydroxy- and amino-modified IONPs predominantly activate the complement system through the LP pathway. We also performed quantitative analysis on the fluid phase activation products C3a and C5a. The highest levels of C3a and C5a were observed in IONP-NH_2^{+44} (Supplementary Fig. 19), these data were consistent with the previous C3b results in Fig. 4F. To better understand the underlying reason for the differences among the three IONPs, we further studied the kinetics of protein adsorption[37]. In our case, the affinity constant (KD) is a measure of the association and dissociation rates between proteins and IONPs. The results of the BLI assay showed a strong affinity of 0.719/1.48 nM between C3b/IgG and IONP-NH_2^{+44}, while few proteins bound directly to IONP-$COOH^{-21}$ or IONP-OH^{-4} (Fig. 4I and Supplementary Fig. 20). Based on these results and previous studies[38–40], we conclude that the IONPs modified with -NH_2 have ability to bind C3b and IgG directly, while the other two IONPs may interact with C3b and IgG indirectly through other factors, including other biomolecular species on the corona.

Surface residues influenced the pharmacokinetics and cellular internalisation of IONPs

The binding of the complement components to IONPs may result in alterations in immune clearance, biodistribution profiles, or cellular uptake efficiency[16]. Therefore, we investigated several crucial pharmacokinetic parameters. The lifetimes of the systemic circulation and biodistribution were shown in Fig. 5A. IONP-$COOH^{-21}$ exhibited the longest half-life of 1.39 h among the tested NPs, and IONP-NH_2^{+44} had the shortest half-life of only 4.41 min (Fig. 5B). These results are consistent with the above results in vitro; IONP-NH_2^{+44} had the highest deposition of C3b and maximum particle size after plasma incubation, thereby accelerating its clearance.

The results of inductively coupled plasma mass spectrometry (ICP-MS) demonstrated that all three IONPs primarily accumulated in the liver (56–80%) and spleen (5–8%) at 24 h post-injection (Fig.5C), which was validated by Prussian blue staining of tissue sections (Supplementary Fig. 21A). However, the distribution in the bone marrow and kidney showed a significant difference; IONP-OH^{-4} showed the lowest distribution in the bone marrow (1.56%) and kidneys (0.9%), by contrast, IONP-NH_2^{+44} displayed obvious distribution in the bone marrow (5.3%), kidneys (7.5%), spleen (8.1%) and lung (3.98%). In addition, no obvious hepatic or renal toxicity was observed, except for elevated ALT levels (>100 IU/L) (Supplementary Fig. 21B).

We also investigated the impact of IONPs on the distribution of immune cells in mice, as depicted in Fig. 5D. IONP-$COOH^{-21}$ treatment maintained the monocytes in peripheral blood, whereas IONP-OH^{-4} was indistinguishable from the saline group. Notably, The IONP-NH_2^{+44} group exhibited distinct characteristics, with $CFSE^+$ cells primarily migrating towards bone marrow upon exposure to nanoparticle stimuli and neutrophils and monocytes displayed particularly pronounced migration (Fig. 5E). Furthermore, the analysis of three additional IONPs in Supplementary Fig. 22 provided further validation of these results. The immune cell distribution induced by IONPs with the same functional modification showed similar patterns.

We conjectured that these variations of IONPs could affect the immune protein opsonization, immune cell uptake and lymphocyte recycle[41–43]. We next investigated the association of immune molecular corona with cell phagocytosis mediated by the complement protein (Fig. 5F, the gating strategy of flow cytometry is available in Supplementary Fig. 23). In both mice and human blood samples, we found distinct uptake patterns of the different IONPs by immune cells. Specifically, IONP-$COOH^{-21}$ exhibited uptake by neutrophils and monocytes selectively, while IONP-NH_2^{+44} was taken up by various immune cells nonselectively, and IONP-OH^{-4} showed negligible uptake by all immune cells with or without EDTA (Fig. 5G and Supplementary Fig. 24). Moreover, C3b opsonisation of IONP-NH_2^{+44} and IONP-$COOH^{-21}$ was reduced by 30–80% in the presence of EDTA, suggesting significant involvement of the complement corona in this process. We further analyzed the correlation between the quality of C3b, circulation half-life and immune cell uptake of three types of IONPs. The results revealed a strong, significant and positive correlation between C3b quality and immune cell uptake. Conversely, a strong negative correlation was observed between C3b quality and circulation half-life (Supplementary Fig. 25). These results indicated that immune uptake of IONPs was influenced by the quantity of the complement components opsonized on NPs. Collectively, these results suggested that the distinct surface residues of IONPs can partially explain the selective responses of various leucocyte classes and their preferential recirculation or migration patterns.

Surface residues-dependent heterogeneity in the immune response to IONPs

To comprehensively evaluate the distinct correlation between immune cell response and surface modifications in vivo, we investigated the dynamic changes of cellular subsets in immune organs, as indicated in Fig. 6A. The distributions and relative frequencies of lymphocytes in spleen were then compared in t-distributed stochastic neighbour embedding analysis (Fig. 6B). Upon administration of IONP-$COOH^{-21}$, there was a significant increase in the number of most immune cell types in both the peripheral blood and spleen after 24 h, which returned to normal levels by 48 h. Moreover, the effects of IONP-OH^{-4} were inert, showing minimal changes in immune cell subsets in both blood and spleen following administration. Conversely, the administration of IONP-NH_2^{+44} resulted in a striking depletion of blood immune cells in C57BL/6N mice at 24 h, and lymphocytes recovered to normal levels by 48 h. Additionally, the absolute count of splenic lymphocytes

https://doi.org/10.1038/s41467-024-54810-0

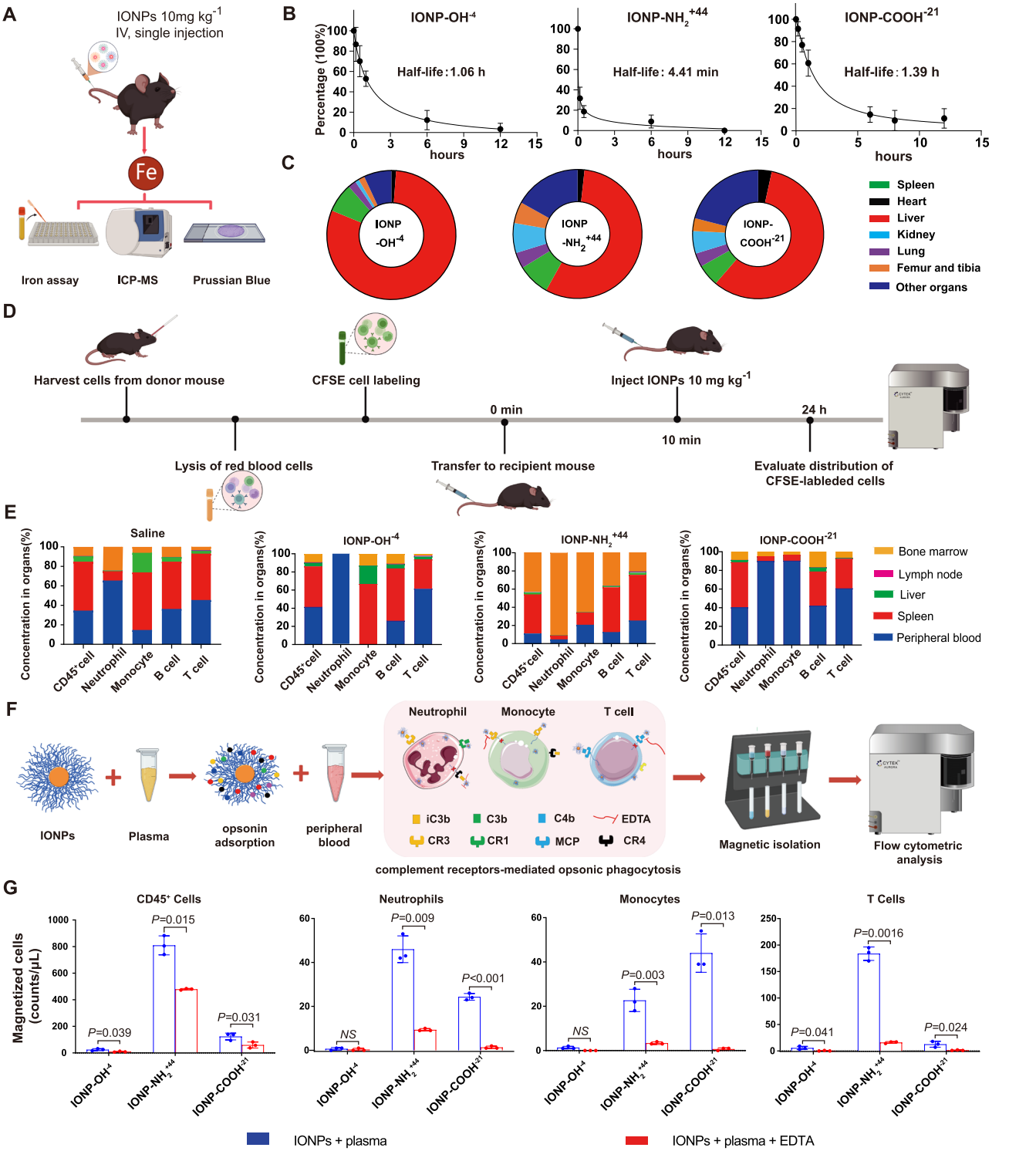

Fig. 5 | Surface residues influenced IONPs' biodistribution, cellular internalisation and the biodistribution of immune cells. A Schematic illustration of experimental workflow (Created in BioRender. Chen, F. (2022) https://BioRender.com/b86y336). **B** The half-lives of IONPs. The sample was collected at different points, and IONPs were determined by iron assay ($n = 6$ mice/group). The $t_{1/2}$ was calculated by nonlinear regression curve fitting. **C** The iron was quantified by inductively coupled plasma mass spectrometry (ICP-MS) ($n = 3$ mice). **D** Schematic illustration for the tracking CFSE labelled peripheral blood immune cells upon IONPs treatment. Created in BioRender. https://BioRender.com/a59b438. **E** Organ relative distribution of $CFSE^+$ peripheral cells ($n = 3$ mice), the experiment was independently repeated twice. **F** Schematic illustration of the experimental setups. **G** The absolute count of immune cells in mouse whole blood ($n = 3$ mice) that phagocytosed plasma-preincubated IONPs. Data are presented as mean ± SD. The experiment was independently repeated twice. A two-tailed *t*-test was used in (**G**). Source data are provided as a Source Data file.

https://doi.org/10.1038/s41467-024-54810-0

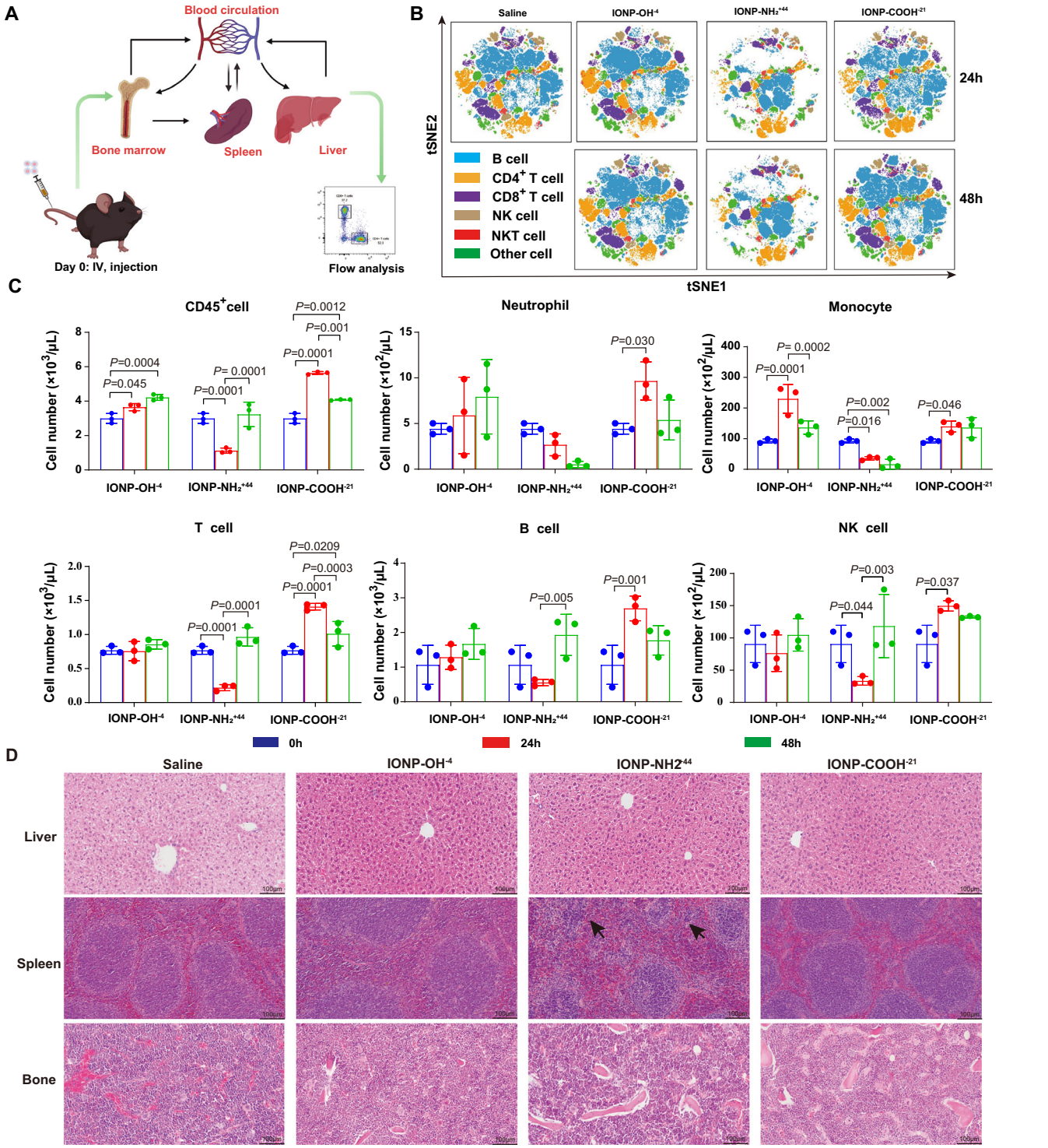

Fig. 6 | Surface residues influenced IONPs' homoeostasis in vivo. A Schematic illustration for in vivo immune system study on C57BL/6N mice given a single dose of 10 mg Fe kg^{-1} IONPs injection (Created in BioRender. https://BioRender.com/h38h965). **B** Visualisation of the major splenocytes using tSNE plots after different IONPs treatments. **C** The number of peripheral WBCs changes following IONP administration, data are presented as mean ± SD, with $n = 3$ mice, experiment was repeated twice independently with similar results. Data were evaluated by two-way ANOVA with multiple comparison adjustments. The flow cytometry gate strategy is shown in Supplementary Fig.12. **D** Representative histological images for tissue sections with hematoxylin and eosin staining (H&E) to evaluate biosafety in vivo. The organs were stained with H&E 24 h after saline or IONP injection. H&E staining showed structural derangement in the spleen (black arrows). Scale bar, 100 μm.

dramatically increased at 24 h and recovered by 48 h after injection of IONP-NH_2^{+44} (Fig. 6B-C and Supplementary Fig. 26A). H&E staining showed structural abnormalities and immune cell infiltration in the spleen and lung of C57BL/6N mice injected with IONP-NH_2^{+44}, such spleen injury may contribute to disease deterioration in Fig. 3C.

These results indicated the peripheral cells migrated toward the liver and spleen after being subjected to nanoparticle stimuli. Notably, a consistent reduction in the number of myeloid cells (neutrophils and monocytes) was observed at 24 h and 48 h post-injection of IONP-NH_2^{+44}. Undoubtedly, these changes led to impaired antiinfection and

antitumour immunity responses, posing a significant limitation for nanoparticle clinical translation. In the bone marrow, progenitor cells characterised by $CD150^{-}$ and $CD48^{+}$ markers increased at 24 h and decreased at 48 h after treatment of IONP-OH^{-4} and IONP-$COOH^{-21}$, while these cells continuously increased up to 48 h in the mice treated with IONP-NH_2^{+44} to compensate for the loss of myeloid cells in the peripheral blood (Supplementary Fig. 26B).

Collectively, these results indicated the heterogeneity of immune response patterns associated with the functional groups of IONPs. From this perspective, our findings provide valuable insights into the possibility of modulating the surface properties of IONPs to regulate their immunological properties, thus enhancing their clinical application in antitumour and antiinfection therapies.

Discussion

Our data demonstrated that IONP-$COOH^{-21}$ effectively impeded the progression of AML and prolonged survival by enhancing phagocytosis of macrophages in a complement C3 dependent manner (Scheme 1). We provided a complete framework for a comprehensive investigation of the intricate interactions between IONPs and the immune system using C57BL/6N and NSG mice, IONP-$COOH^{-21}$ inhibited leukaemia development through elevating phagocytic ability of macrophages and facilitating T cell-mediated adaptive immune response base on complement C3 in corona but not ferroptosis (Supplementary Fig. 27, 28) demonstrated in previous report[28]. The depletion of macrophages through clodronate-liposome and the use of C3 knockout mice further confirmed the effector cells and molecular mechanisms contributing to elucidate the antileukaemia effects of IONP-$COOH^{-21}$. Our observations underscore the potential of IONP-$COOH^{-21}$ as a promising candidate for AML treatment by boosting antitumour immunity irrespective of the ferroportin expression in AML cells.

The complement components present in the biomolecular corona emerged as a pivotal role in driving the ensuing immune response. The PC on NPs is primarily responsible for regulating NPs' cellular recognition, uptake and subsequent responses, the strategic assembly of functional protein on NPs surfaces can promote precise triggering of specific immune cell subsets and modulate both the timing and intensity of immune activation, thereby improving the precision of immune response. However, the dynamic process of interactions of nanoparticle-protein complex with immune cells need to be further investigated.

To address the potential roles of the functional group modification on NPs in regulating PC formation and subsequent immune response, the carboxyl, amino and hydroxyl modified IONPs were assessed for their abilities in regulating PC assemble, immune activation and biosafety in vivo. The results showed that carboxyl modified IONPs exhibit good biosafety profiles with a prolonged half-life, activate complement alternative pathway and lead to subsequent immune cell activation. In contrast, IONP-NH_2 triggered the lectin pathway and resulted in immune cell depletion, while IONP-OH did not exhibit discernible immune regulation effects. These results revealed the critical roles of surface modification in assembling immunological PC and subsequent immune response to IONPs in vivo, but there is also a need for more follow-up studies to assess other physicochemical properties of iron oxide NPs, such as size, precise compositions and chemical stability.

In our study, complement pathway experiments were conducted using samples derived from AML patients, while phagocytosis-related experiments were performed on mice. The translational value of these findings requires careful consideration of species-specific differences in complement-opsonization and phagocytosis mechanisms. For instance, Li et al. demonstrated that iron oxide NPs primarily activate the complement system through the lectin pathway in mice, whereas in humans, the alternative pathway is more prominently involved[36]. This is consistent with the results of our study in the patient sample. Furthermore, C3b-mediated phagocytosis, a critical process studied in our research, also shows interspecies variations. While CR3 is conserved across species[44,45], there are some differences between humans and mice in terms of CR3 expression levels and functions. Erdei et al.

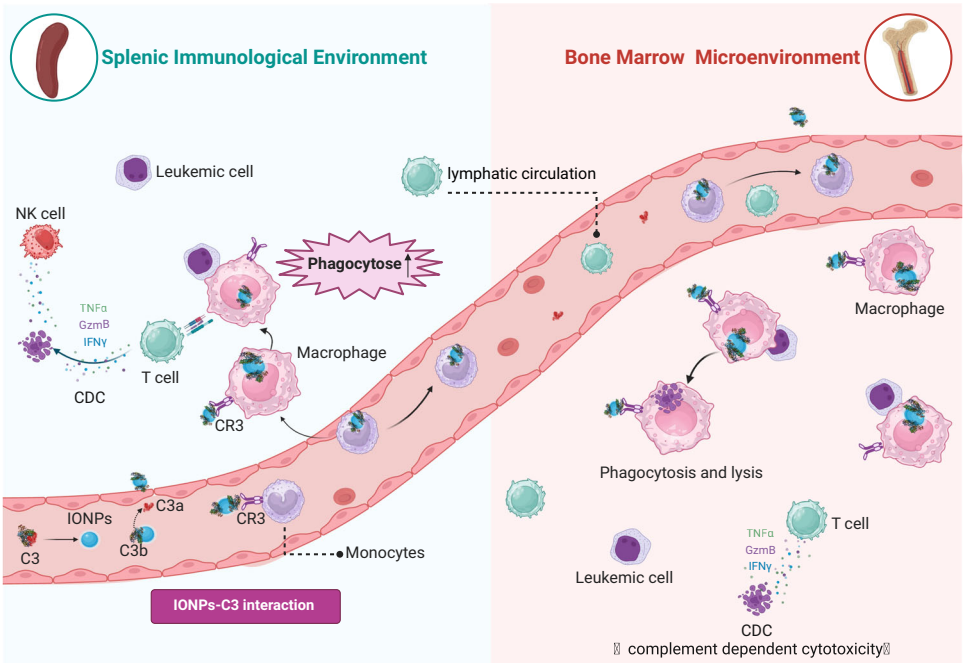

Scheme 1 | Nanoparticles dynamically interact with immune cells via complement corona to exert antileukaemia efficacy. The interactions that occur at the IONPs-complement interface play a vital role in determining the immunological effects. IONP could adopt complement C3b, thereby bind to the C3 receptor (CR3) of the circulating monocytes. The activated circulating monocytes migrated to immune organs and differentiatied into resident macrophages, at the same time, IONPs-C3b complex potentiated the phagocytosis of leukaemia cells by resident macrophages. Furthermore, macrophages can present tumour antigens to T cells, subsequently activated adaptive antileukaemia immunity (Created in BioRender. Chen, F. (2023) https://BioRender.com/z95h917).

highlighted that, although CR3 mediates overlapping functions in monocytes, and macrophages of both species, the expression levels and specific roles can differ significantly. For instance, human myeloid cells show higher CR3 expression compared to murine cells, which can influence the efficiency of phagocytosis mediated by C3b-opsonization[46]. Given that our observations were manifest in murine subjects, they may potentially exhibit greater applicability in the context of AML patients. However, further validation in human-specific systems is essential for accurate translation to clinical applications. Complement serves as a crucial mediator for the entry of IONPs into immune cells. Upon their internalisation, IONPs not only alter phagocytic activity but may also elicit additional cellular responses, including oxidative stress and metabolic changes. Further research is imperative to understand the broader implications of these changes on immune responses. Overall, these discoveries not only deepen the understanding of nanomaterial-immune system interactions but also pave the way to utilise NPs rationally and develop immunotherapies against various cancers. Moreover, given the fact that ferumoxytol is an intravenous iron oxide nanoparticle formulation that has been approved by the FDA, it could be rapidly incorporated into clinical trials for cancer immunotherapy.

Methods

Ethics statement

The human study was approved by the Medical Ethics Committee of China-Japan Union Hospital of Jilin University (Approval No.: 2019040811). Plasma samples were provided by the Department of Laboratory Medicine or the Physical Examination Center at China-Japan Union Hospital of Jilin University. Written informed consent was obtained from all participants in accordance with the Declaration of Helsinki, and all samples were de-identified to ensure patient confidentiality. Samples were exclusively utilised for the purposes of this study. This study included male and female participants without restriction on sex or gender. Animal experiments were approved by the Institutional Animal Care and Use Committee (ACUC) of Jilin University (Approval No.: 2022-470) and were conducted in compliance with institutional and national ethical guidelines for animal care and use.

Participant selection and sample collection

This study included blood samples from healthy donors ($n = 10$) and patients with AML ($n = 6$). All participants were aged between 18 and 65 years and included both male and female individuals. Healthy donors were defined based on self-reported good health status and confirmation that routine blood test parameters were within normal reference ranges. Blood samples from healthy donors were obtained to investigate whether the interactions between human immune cells and nanomaterials with different surface functional groups follow the patterns observed in animal models. This analysis is critical for evaluating the clinical translational potential of these nanomaterials. Samples from AML patients were collected to examine the characteristics of PC formation on nanomaterial surfaces under disease conditions. Insights into these disease-specific PC features can guide the development of personalised therapeutic applications for nanomaterials in AML. This study was approved by the Medical Ethics Committee of China-Japan Union Hospital of Jilin University and conducted in accordance with the guidelines of the Institutional Review Board and the Declaration of Helsinki. All participants provided written informed consent. No financial compensation was provided to the participants.

Cell lines and animal care

Murine leukaemia cell line BCR-Nup (from female mouse) and human leukaemia cell lines MOLM-13 (from male patient) were gifted by Dimitri Simberg's lab (University of Colorado Anschutz Medical Campus, USA), and mycoplasma testing was performed on all cell lines. The MOLM-13 cell line was derived from a male patient with AML. The BCR-Nup cell line, derived from female mice, was created by co-expressing BCR-ABL and NUP98-HOXA9 fusion genes. Cells were cultured in RPMI 1640 medium (Gibco) supplemented with 10% heat-inactivated foetal bovine serum and 1% antibiotics (penicillin-streptomycin, 100 U mL^{-1}) at 37 °C, 5% CO_2. C57BL/6N mice (males, 8 weeks old) and NOD-Prkdc^{scid}Il2rg^{em1}/Smoc (NSG) mice were purchased from Beijing Vital River Laboratory Animal Technology and Shanghai Model Organisms Center Inc., respectively. C3-knockout mice (B6.129S4-C3tm1Crr/J) were gifted by Shaojun Xing (Shenzhen University Health Science Center, China). All mice were housed at a maximum of five animals per cage with fluid and food ad libitum, on a 12 h dark/light cycle, at ambient temperature and relative humidity of 45–65%. All protocols were approved by the College of Basic Medical Sciences, Jilin University and performed under the ethical guidelines for the use and care of animals.

Iron oxide nanoparticles

IONP-COOH^{-21} (Feraheme®) was acquired from the University of Colorado Hospital Pharmacy. IONP-COOH^{-21} is an FDA-approved drug for the treatment of iron deficiency in renal impaired patients. For this study, we utilised a range of nanoparticle materials, each identified by specific product codes to ensure precise reproducibility and traceability. The following NPs were employed: CL-50Q02-6A-0, CL-50Q01-6A-50, CL-30Q02-2, CL-30Q02-6 and CL-30Q02-6C. These materials were purchased from the Biophysics Assay Laboratory (USA), ensuring high quality and consistency across experiments. All iron oxide nanoparticles (IONPs) with an iron oxide core and a 10 Kda dextran coating have a mean hydrodynamic diameter of 30 nm.

Characterisation of nanoparticles

The morphology and structure of the materials were characterised using various physicochemical techniques, including TEM, DLS and XPS. The Zetasizer Nano ZS (Malvern Instruments) was used to test the size and zeta potential of IONPs. TEM imaging was used to visualise IONPs by a JEM-2100F transmission electron microscope (Electron Microscopy Center, Jilin University, CN). An XPS was conducted on an Escalab-250 instrument (Thermo Fisher Scientific, Waltham, MA, USA) with a hemisphere detector and a monochromatic Al Kα radiation source (1486.6 eV).

To prepare the IONPs for infrared spectroscopy analysis, a 50 µL aliquot of IONPs at a concentration of 2 mg/mL underwent a lyophilization process at −20 °C for 48 h to remove solvent and stabilise the particles. Subsequently, the lyophilised samples were transferred to a vacuum dryer and subjected to further drying for 72 h to ensure complete removal of residual moisture, thereby preventing any interference in the infrared spectra. The dried IONP samples were then analyzed using Fourier-transform infrared spectroscopy (FTIR) on a BRUKER instrument housed at the State Key Laboratory of Superhard Materials, Jilin University. This methodological approach guarantees the absence of water-related artifacts and facilitates precise characterisation of the nanoparticle surface chemistry and functional groups.

Proteomics analysis

Label-free mass spectrometry was conducted to determine the surface proteins of IONPs. A total of six IONP samples were analyzed with biological replicates ($n = 1$). IONPs (100 µL, 1 mg Fe/mL) were incubated with healthy human plasma (300 µL) for 30 min at 37 °C in 1.5 mL tubes (Beckman-Coulter, Brea, CA). IONPs were washed 3 times at 4 °C by Beckman Optima Ultracentrifuge (TLA-100.3 rotor, 70,000 × g, 25 min). The proteins were eluted with 2% SDS-100 mM Tris-Hcl for 10 min at 95 °C[20,21,47]. BCA Protein Assay (Thermo Fisher Scientific, Waltham, MA, US) was performed to test the protein concentration. The LC-MS/MS analysis was conducted by Shanghai OE Biotech Co., Ltd. All analyses were performed by a QE mass spectrometer (Thermo Fisher Scientific,

USA) equipped with an Easyspray source (Thermo, USA). Samples were loaded by a capillary trap column (100μm×2 cm, RP-C18, Thermo Fisher) and then separated by a capillary analytical column (15 cm × 75 μm, RP-C18, Thermo Fisher Scientific) on an EASY-nLCTM 1200 system (Thermo, USA). The MS data were analyzed for protein identification and quantification using ProteinPilot software (v.5.0) and sequence database (uniport reviewed_yes+taxonomy_9606.fasta), specific steps are detailed in the Supplementary Fig. 29.

Identification of the proteins adsorbed onto the IONPs

To detect the binding of complement, we mixed IONPs (1 mg mL^{-1}) with healthy human and AML patients plasma at a 1:3 (vol/vol) ratio with or without complement inhibitors (10 mM EDTA) at 37 °C for 30 min. IONPs were washed three times with pre-cooled 10 mM PBS without calcium and magnesium (pH 7.4) and centrifugated at 70,000 × *g* at 4 °C in PBS using a Beckman Optima TLX Ultracentrifuge. The pellets were resuspended in 20 μl PBS and analyzed by dot blot for bound C3b/P or Western blot for bound C4b and Bb. In Fig. 4H, the dot blot fluorescence intensity, represented by the dots on the bar chart, indicates the total amount of C3b and properdin bound to the IONP. The height of each bar corresponds to the number of C3b molecules per IONP, calculated by first quantifying the total number of IONPs in each dot blot using Nanosight Tracking Analysis (NTA). This method ensures precise measurement of the average number of C3b molecules adhered to each IONP. The specific method was described in a previous study[24]. Supernatants were collected to measure C1s/C1-INH complex (Hycult Biotech, HK399), MASP1/C1-INH complex (Hycult Biotech, HK3001), C3a and C5a using the Human C3a ELISA Kit (Invitrogen, BMS2089) and Human C5a ELISA Kit (Abcam, ab193695), respectively.

Iron quantification

IONPs dispersed in saline were IV injected into male C57BL/6N mice at a dose of 10 mg Fe kg^{-1}. The peripheral blood was taken at once, 1 min, 10 min, 30 min, 1 h, 6 h, 12 h, 24 h and 48 h post-IONPs injection. The iron content was assessed using iron assay[21,47,48] and measured using absorbance at 600 nm (background absorption of the blood was subtracted). In addition, to evaluate the biodistribution of IONPs in vivo, fully dried liver, kidney, spleen, heart, unilateral tibiae and lung were digested in aqua regia for ICP-MS analysis. Its detailed steps were as follows: collected tissues were carefully washed in double-distilled water, weighed, frozen and subsequently freeze-dried and homogenised. Then samples were mineralised by wet digestion by using a constant temperature (90 °C) metal bath and reacted for 6 h in 500 μL aqua regia. After digestion, we transferred the samples into 10 mL tubes and added them with deionized water. The above operation was performed in a well-vented fume hood.

IONP uptake by leucocytes

IONPs were incubated with healthy mice or human plasma, we added EDTA (10 mM) to the plasma before adding IONPs to inhibit the complement. After each incubation step, IONPs were incubated with cells in the metal bath at 37 °C for 40 min at 500 rpm. Then washed with saline, the cells which uptake IONPs were isolated by MiniMACS magnetic columns (Miltenyi Biotec, Bergisch Gladbach, DE). Subsequently, single cell suspensions were then stained with fluorescent-conjugated antibodies and identified by Cytek Flow Cytometer NL-3000 (Cytek BioSciences, Freemont, CA, US) using Cytek SpectroFlo software.

Adoptive transfer

For cell distribution tracking, the peripheral blood of 8-week-old male C57BL/6N mice was collected and treated with 1 × erythrocytes lysate in aseptic conditions. 2×10^6 cells were stained with CFSE and transferred into recipient mice via intravenous injection. After 10 min of circulation, recipient mice received either IONPs in saline solution with the same dose or equal volume saline injection and were sacrificed 24 h later. The $CFSE^+$ cells in the harvested organ were re-collected and analyzed by flow cytometry to observe the effects of IONPs on peripheral blood immune cell distribution.

Animal models

Immunity model. C57BL/6N mice (male and female, 8 weeks old) were purchased from Beijing Vital River Laboratory Animal Technology, Beijing, CN. Animals were randomly allocated by investigators to experiment groups using a random number table at once to minimise bias. The experimental group received a single injection (IV) of 10 mg kg^{-1} of IONPs or saline in a total volume of 150 μL. Mice were anesthetized and peripheral blood samples were collected from the retro-orbital venous plexus with heparin-coated capillary tubes at various time points after injection for flow cytometry analysis. Similarly, the organs of mice were harvested at 24 and 48 h after injection. All tissue samples were divided into three pieces, weighed and processed for flow cytometry, histopathology and ICP-MS.

Xenograft model. Eight-week-old male and female NOD/SCID IL-2R gamma null (NSG) mice were purchased from the Shanghai Model Organisms Center (Shanghai, CN). The experimental procedures were approved by the Animal Care and Use Committee of Jilin University. To establish the AML model in our study, NSG mice were injected with human leukaemia cells (0.5 million MOLM13 cells /mouse, IV). The presence of leukaemia blasts was determined by flow cytometry. The mice were randomly divided into different groups ($n = 10$) for survival studies when 0.1% of the tumour burden was detected in peripheral blood, (Investigators were not blinded to the therapy that mice were receiving). Various treatments were administered intravenously at 6 mg of Fe per kg body weight every 3 days for a total of three injections. The mice were euthanized at the indicated times or with signs of breathing disorders, weight loss, or immobility.

Syngeneic model. C57BL/6N mice (male, 8 weeks old) and C3-knockout mice (B6.129S4-C3tm1Crr/J) were given with tumour cells. And treated with saline or IONPs 6/10 mg kg^{-1} on days 3 and 8. Flow cytometry analyses of leukaemia cells were detected on day 10.

From the seventh day post-modelling, all animals were monitored daily for body weight and bone marrow leukaemia burden. Humane euthanasia was performed at designated time points or when signs of distress were observed, including laboured breathing, paralysis of hind limbs, inability to eat or drink, or body weight loss exceeding 20%. The leukaemia burden in bone marrow was not permitted to exceed 80%, as specified by the institutional ethical guidelines. We confirm that no tumour exceeded this limit during the study. Humane endpoints were applied according to established institutional protocols, with defined criteria including body weight loss, clinical signs of distress and leukaemia burden limits. All procedures were regularly reviewed by the Institutional Animal Care and Use Committee (IACUC) to ensure ongoing compliance with ethical standards and the latest institutional requirements.

Macrophage depletion

C57BL/6N mice (male, 8 weeks old) were injected (IP) with 0.15 mL of control liposomes or clodronate liposomes (FormuMax Scientific, # F70101-N) on day -1. and 5×10^4 BCR-Nup cells were inoculated on day 0, while liposomes were injected as a control. On day 1, $CD11b^+$ $F4/80^+$ macrophages (negative for CD19, CD3 and Ly6G) in different organs were analyzed by flow cytometry. $IONP\text{-}COOH^{-21}$ treatment was performed on day 11 and the mice were euthanized on day 12,

Phagocytosis assays

Primary peritoneal macrophages were obtained using peritoneal lavage with 5 ml of sterile saline from C57BL/6N mice (male, 8 weeks old) and isolated by the adherent method. The macrophages were plated at 2×10^5 per well in 24-well plates with 500 μl of medium per well, and the medium was changed 5 h later. After standing overnight,

the preincubated IONP-COOH^{-21} with specific plasma proteins (whole plasma proteins or C3-depleted plasma) was added and stimulated for 1 h. After 5 h, MOLM-13 cells were labelled with CFDA SE (Beyotime, # C1031,1:50000 dilutions) and cocultured (1×10^6 per well) with macrophages at 37 °C for 2 h. And macrophages were detached with Accutase® Cell Detachment Solution (BioLegend, # 423201), and analyzed by flow cytometry after labelling with F4/80 antibody. Quantification was based on 3 samples of each group and at least of 5 random fields of view per sample; pictures were acquired using a ZEISS Axiocam 202 mono microscope camera.

Flow cytometry

The immunostimulatory potential of IONPs in immunity model. To evaluate the immunostimulatory effect of NPs in vivo, peripheral blood, spleen, liver and bone marrow were obtained at the indicated times. The spleen was dissected from mice and ground in 3 mL ice-cold PBS with 2% FBS, then filtered tissues through a 70-μm diameter nylon mesh to generate a single-cell suspension. The single cell suspension was collected and centrifuged at $450 \times g$ at 4 °C for 5 min, then cells were resuspended in PBS with 2% FBS. Hereinto, 50 μL cell suspension was used for flow staining. Bone marrow was flushed out of the femur with 1 mL ice-cold PBS with 2% FBS, filtered by a 70-mm cell strainer and cell suspension was aspirated for flow staining. Thereafter, a variety of cells were incubated for 10 min at room temperature with Fc Receptor Binding Inhibitor (#156603, BioLegend, San Diego, CA, US), True-Stain Monocyte Blocker (#426103, BioLegend) and Brilliant Stain Buffer (#566349, BD Biosciences) to exclude nonspecific staining. After that, peripheral blood cells were incubated with antibodies.

Leukaemia burden evaluation in a disease model. Cells in bone marrow were stained with antihuman CD45 and antimouse CD45 to evaluate tumour cell engraftment. Tumour cells were determined by detecting the percentage of hCD45$^+$mCD45$^-$ cells. Cells were evaluated in a Cytek Flow Cytometer NL-3000 (Cytek BioSciences). And GFP$^+$ represented leukaemic cells in the syngeneic model. For the detailed list of antibodies used, see Supplementary Table 1.

Statistics & reproducibility

All data are presented as mean ± SD, and statistical analysis and graphs were performed using GraphPad Prism software (GraphPad Software, San Diego, CA, US) and SPSS programme for Windows (SPSS 15.0; SPSS Inc), with flow cytometry data analyzed using Flow Jo V10. The number (n) and type (biological or technical) of replicates are indicated in the figure legends. Each in vitro experiment was performed in at least 3 replicates and 2 repetitions. For all in vivo experiments, n is indicated for each in the manuscript for independent biological replicates. Multiple samples were obtained per experimental mouse at their respective experimental endpoints experiments and each data point indicates one replicate on graphs. In vivo experiments included 2 repetitions. The experiments were randomised, and investigators were not blinded to allocation during experiments and outcome assessment. No statistical method was used to predetermine sample size. The sample sizes in this study were chosen based on standards observed in previous similar studies, with all data points representing biological replicates (distinct experimental subjects). Results were consistent across repeated experiments. For all data, normality was first assessed. If the data followed a normal distribution, we applied one-way ANOVA for multiple group comparisons and a two-tailed unpaired Student's *t*-test for two group comparisons. If the data did not follow a normal distribution, the Mann-Whitney U test was used for two group comparisons, and the Kruskal-Wallis test was employed for multiple group comparisons. A P value less than 0.05 was considered significant (NS: $P > 0.05$, represents non-significance), and all P values were two-tailed. No data were excluded from the analyses.

Reporting summary

Further information on research design is available in the Nature Portfolio Reporting Summary linked to this article.

Data availability

The mass spectrometry proteomics data generated in this study have been deposited in the ProteomeXchange Consortium via the iProX partner repository under accession code PXD056769[49,50]. https://www.iprox.cn/page/home.html. The source data generated in this study are provided in the Source Data file. Source data are provided with this paper.

References

1. Romero, A. et al. Clinical Characteristics of Chilean Adult Patients with Acute Myeloid Leukemia (AML): Analysis within the Framework of the Epidemiological Registry of AML of the Pethema Group. *Blood* **140**, 8963–8965 (2022).
2. Newell, L. F. & Cook, R. J. Advances in acute myeloid leukemia. *BMJ* **375**, n2026 (2021).
3. Surapally, S., Tenen, D. G. & Pulikkan, J. A. Emerging therapies for inv (16) AML. *Blood* **137**, 2579–2584 (2021).
4. Yi, M. et al. The global burden and attributable risk factor analysis of acute myeloid leukemia in 195 countries and territories from 1990 to 2017: estimates based on the global burden of disease study 2017. *J. Hematol. Oncol.* **13**, 72 (2020).
5. Ci, T. et al. Delivery strategies in treatments of leukemia. *Chem. Soc. Rev.* **51**, 2121–2144 (2022).
6. Wang F. et al. Iron and leukemia: new insights for future treatments. *J. Exp. Clin. Cancer Res.* **38**, 406 (2019).
7. Li, J. et al. Development and application of nanomaterials, nanotechnology and nanomedicine for treating hematological malignancies. *J. Hematol. Oncol.* **16**, 65 (2023).
8. Liu, Y. et al. Nano-Bio interactions in cancer: from therapeutics delivery to early detection. *Acc. Chem. Res.* **54**, 291–301 (2021).
9. Zhang, P. et al. Nanotechnology-enhanced immunotherapy for metastatic cancer. *Innovation* **2**, 100174 (2021).
10. Wang, X. & Zhang, W. The Janus of Protein Corona on nanoparticles for tumor targeting, immunotherapy and diagnosis. *J. Control Release* **345**, 832–850 (2022).
11. Zanganeh, S. et al. Iron oxide nanoparticles inhibit tumour growth by inducing pro-inflammatory macrophage polarization in tumour tissues. *Nat. Nanotechnol.* **11**, 986–994 (2016).
12. Zhao, J. et al. Anti-tumor macrophages activated by ferumoxytol combined or surface-functionalized with the TLR3 agonist poly (I: C) promote melanoma regression. *Theranostics* **8**, 6307–6321 (2018).
13. Stater, E. P., Sonay, A. Y., Hart, C. & Grimm, J. The ancillary effects of nanoparticles and their implications for nanomedicine. *Nat. Nanotechnol.* **16**, 1180–1194 (2021).
14. Lee, H. Effects of nanoparticle electrostatics and protein-protein interactions on corona formation: conformation and hydrodynamics. *Small* **16**, e1906598 (2020).
15. Li, M. et al. Nanoparticle elasticity affects systemic circulation lifetime by modulating adsorption of apolipoprotein A-I in corona formation. *Nat. Commun.* **13**, 4137 (2022).
16. Lundqvist, M. et al. Nanoparticle size and surface properties determine the protein corona with possible implications for biological impacts. *Proc. Natl. Acad. Sci. USA* **105**, 14265–14270 (2008).
17. Vincent, M. P. et al. Surface chemistry-mediated modulation of adsorbed albumin folding state specifies nanocarrier clearance by distinct macrophage subsets. *Nat. Commun.* **12**, 648 (2021).
18. Cedervall, T. et al. Understanding the nanoparticle–protein corona using methods to quantify exchange rates and affinities of proteins for nanoparticles. *Proc. Natl. Acad. Sci. USA* **104**, 2050–2055 (2007).

19. Li, J. et al. Precision design of engineered nanomaterials to guide immune systems for disease treatment. *Matter* **5**, 1162–1191 (2022).
20. Vu, V. P. et al. Immunoglobulin deposition on biomolecule corona determines complement opsonization efficiency of preclinical and clinical nanoparticles. *Nat. Nanotechnol.* **14**, 260–268 (2019).
21. Chen, F. et al. Complement proteins bind to nanoparticle protein corona and undergo dynamic exchange in vivo. *Nat. Nanotechnol.* **12**, 387–393 (2017).
22. Ke, P. C., Lin, S., Parak, W. J., Davis, T. P. & Caruso, F. A decade of the protein corona. *ACS Nano* **11**, 11773–11776 (2017).
23. Ali, H. & Panettieri, R. A. Anaphylatoxin C3a receptors in asthma. *Respir. Res.* **6**, 19 (2005).
24. Guo, R. F. & Ward, P. A. Role of C5a in inflammatory responses. *Annu. Rev. Immunol.* **23**, 821–852 (2005).
25. Vandendriessche, S., Cambier, S., Proost, P. & Marques, P. E. Complement receptors and their role in leukocyte recruitment and phagocytosis. *Front. Cell Dev. Biol.* **9**, 624025 (2021).
26. Bournazos, S., Gupta, A. & Ravetch, J. V. The role of IgG Fc receptors in antibody-dependent enhancement. *Nat. Rev. Immunol.* **20**, 633–643 (2020).
27. Nimmerjahn, F. & Ravetch, J. V. Fcgamma receptors as regulators of immune responses. *Nat. Rev. Immunol.* **8**, 34–47 (2008).
28. Trujillo-Alonso, V. et al. FDA-approved ferumoxytol displays anti-leukaemia efficacy against cells with low ferroportin levels. *Nat. Nanotechnol.* **14**, 616–622 (2019).
29. Ashton, J. M. et al. Gene sets identified with oncogene cooperativity analysis regulate in vivo growth and survival of leukemia stem cells. *Cell Stem Cell* **11**, 359–372 (2012).
30. Ye, H. et al. Leukemic stem cells evade chemotherapy by metabolic adaptation to an adipose tissue niche. *Cell Stem Cell* **19**, 23–37 (2016).
31. Khan, M. A., Assiri, A. M. & Broering, D. C. Complement and macrophage crosstalk during process of angiogenesis in tumor progression. *J. Biomed. Sci.* **22**, 58 (2015).
32. Ricklin D., Mastellos D. C., Lambris J. D. Therapeutic targeting of the complement system. *Nat. Rev. Drug. Discov*. https://www.nature.com/articles/s41573-019-0055-y (2019).
33. Alves da Silva, P. H. et al. MICA/B antibody induces macrophage-mediated immunity against acute myeloid leukemia. *Blood* **139**, 205–216 (2022).
34. Śledzińska, A. et al. Regulatory T cells restrain interleukin-2- and Blimp-1-dependent acquisition of cytotoxic function by CD4 T cells. *Immunity* **52**, 151–166.e6 (2020).
35. Burke, J. D. & Young, H. A. IFN-γ: a cytokine at the right time, is in the right place. *Semin. Immunol.* **43**, 101280 (2019).
36. Li, Y. et al. Complement opsonization of nanoparticles: differences between humans and preclinical species. *J. Control. Release* **338**, 548–556 (2021).
37. Ren, J. et al. Chemical and biophysical signatures of the protein corona in nanomedicine. *J. Am. Chem. Soc.* **144**, 9184–9205 (2022).
38. Ren, J. et al. Precision nanomedicine development based on specific opsonization of human cancer patient-personalized protein coronas. *Nano Lett.* **19**, 4692–4701 (2019).
39. Huynh, A., Kelton, J. G., Arnold, D. M., Daka, M. & Nazy, I. Antibody epitopes in vaccine-induced immune thrombotic thrombocytopaenia. *Nature* **596**, 565–569 (2021).
40. Jung, V. et al. BLI-MS: Combining biolayer interferometry and mass spectrometry. *Proteomics* **22**, e2100031 (2022).
41. Francia, V. et al. Corona composition can affect the mechanisms cells use to internalize nanoparticles. *ACS Nano* **13**, 11107–11121 (2019).
42. Ju, Y. et al. Person-specific biomolecular coronas modulate nanoparticle interactions with immune cells in human blood. *ACS Nano* **14**, 15723–15737 (2020).
43. Zhang, Y., Wu, J. L. Y., Lazarovits, J. & Chan, W. C. W. An analysis of the binding function and structural organization of the protein corona. *J. Am. Chem. Soc.* **142**, 8827–8836 (2020).
44. Eddy, A., Newman, S. L., Cosio, F., LeBien, T. & Michael, A. The distribution of the CR3 receptor on human cells and tissue as revealed by a monoclonal antibody. *Clin. Immunol. Immunopathol.* **31**, 371–389 (1984).
45. Ji, H.-B. et al. T cell-specific expression of the murine CD3delta promoter. *J. Biol. Chem.* **277**, 47898–47906 (2002).
46. Erdei, A. et al. Non-identical twins: different faces of CR3 and CR4 in myeloid and lymphoid cells of mice and men. *Semin Cell Dev. Biol.* **85**, 110–121 (2019).
47. Simberg, D. et al. Differential proteomics analysis of the surface heterogeneity of dextran iron oxide nanoparticles and the implications for their in vivo clearance. *Biomaterials* **30**, 3926–3933 (2009).
48. Wang, G. et al. High-relaxivity superparamagnetic iron oxide nanoworms with decreased immune recognition and long-circulating properties. *ACS Nano* **8**, 12437–12449 (2014).
49. Ma, J. et al. iProX: an integrated proteome resource. *Nucleic Acids Res.* **47**, D1211–D1217 (2019).
50. Chen, T. et al. iProX in 2021: connecting proteomics data sharing with big data. *Nucleic Acids Res.* **50**, D1522–D1527 (2022).

Acknowledgements

The authors sincerely thank Professor Xiaoli Huang and her doctoral student Yuchen Zhang from the State Key Laboratory of Superhard Materials at Jilin University for their invaluable assistance with infrared spectroscopy detection and analysis. The authors acknowledge Shanghai OE Biotech Co., Ltd. (Shanghai, China) for their support in conducting quantitative proteomic analysis and functional analysis of proteins. The authors acknowledge Biorender for providing the software that enabled us to create the schematic diagrams presented in this work. This work was supported by the National Key Research and Development Program (2021YFC2400600/2021YFC2400603) (F.C.), the National Natural Science Foundation of China (32271446, 31771093) (F.C.), Program of Health Department of Jilin Province (2022SCZ26, 2022JC075, 2022LC121) (F.C.), Norman Bethune Program of Jilin University (2022B21, 2022B37) (F.C.), The China Postdoctoral Science Foundation (2022TQ0118, 2022M721309) (F.C.), The Natural Science Foundation of Jilin Province (YDZJ202101ZYTS024, YDZJ202301-ZYTS427) (F.C.), Development and Reform Commission Foundation of Jilin Province (2019C023) (F.C.), Finance Department Foundation of Jilin Province (2020SCZ61) (F.C.), the Programme for JLU Science and Technology Innovative Research Team (JLUSTIRT, 2019TD-36) (F.C.), the Natural Science Foundation of Jilin Province (YDZJ202101ZYTS024) (F.C.). The funders had no role in study design, data collection and analysis, decision to publish, or preparation of the manuscript.

Author contributions

F.C. contributed to the study conception and design. Y.L. (Yuanyuan Li), W.W. and Q.L. contributed to material preparation, data collection, methodology, formal analysis and visualisation. Q.W. and Y.Z. were responsible for material characterisation. P.R. and H.L. provided the test samples. J.Z., Y.L. (Yuanyuan Lv), B.T., S.S., J.C. and J.W. were responsible for conducting the animal experiments. X.X. was responsible for performing and analysing the BLI assays of protein molecules interacting with nanomaterials in vitro. W.Z. and Z.W. were responsible for the transmission electron microscopy characterisation of the nanomaterials. The first draft of the manuscript was written by Y.L. (Yuanyuan Li). Q.L., F.C. and M.G. supervised the writing. All the other authors revised and commented on previous versions of the manuscript. F.C. is the study guarantor and attests that all listed authors meet authorship criteria and that no others meeting the criteria have been omitted. All authors read and approved the final manuscript.

Competing interests
The authors declare no competing interests.

Additional information
Supplementary information The online version contains supplementary material available at https://doi.org/10.1038/s41467-024-54810-0.

Correspondence and requests for materials should be addressed to Fangfang Chen.

Peer review information *Nature Communications* thanks Jan Grimm, Morteza Mahmoudi, Per Nilsson and the other, anonymous, reviewer(s) for their contribution to the peer review of this work. A peer review file is available.

Reprints and permissions information is available at http://www.nature.com/reprints

Publisher's note Springer Nature remains neutral with regard to jurisdictional claims in published maps and institutional affiliations.

Open Access This article is licensed under a Creative Commons Attribution-NonCommercial-NoDerivatives 4.0 International License, which permits any non-commercial use, sharing, distribution and reproduction in any medium or format, as long as you give appropriate credit to the original author(s) and the source, provide a link to the Creative Commons licence, and indicate if you modified the licensed material. You do not have permission under this licence to share adapted material derived from this article or parts of it. The images or other third party material in this article are included in the article's Creative Commons licence, unless indicated otherwise in a credit line to the material. If material is not included in the article's Creative Commons licence and your intended use is not permitted by statutory regulation or exceeds the permitted use, you will need to obtain permission directly from the copyright holder. To view a copy of this licence, visit http://creativecommons.org/licenses/by-nc-nd/4.0/.

© The Author(s) 2024